Selective Phosphate Removal with Manganese Oxide Composite Anion Exchange Membranes in Membrane Capacitive Deionization

Bin Yang[a], Xiaoliu Zhang[b], Bharat Shrimant[a], Tanmay Kulkarni[a], Revati Kumar[b]*, Christopher G. Arges[a,*,⊥]

[a]Department of Chemical Engineering, Pennsylvania State University, University Park, PA 16802, USA

[b]Department of Chemistry, Louisiana State University, Baton Rouge, LA 70803, USA.

*Corresponding authors' emails: chris.arges@psu.edu, revatik@lsu.edu

[⊥]Current address and email: Argonne National Laboratory, Lemont, IL 600439, carges@anl.gov

ABSTRACT

The discharge of excessive phosphorous into water bodies can lead to serious eutrophication threatening aquatic ecosystem. Membrane capacitive deionization (MCDI) is an effective platform for deionizing aqueous streams; however, conventional MCDI is unable to selectively remove targeted ions from a liquid mixture. In this work, we fabricated manganese oxide composite anion exchange membranes (AEMs) for MCDI to enhance phosphate removal selectivity from sodium chloride-sodium dihydrogen phosphate (10:1 molar ratio) aqueous mixtures. We systematically investigated several critical factors, such as constant current or voltage operation, applied voltage amount, process stream pH, and manganese oxide content in the AEM, on phosphate removal efficiency and phosphate selectivity. A trade-off was observed between phosphate removal and selectivity when increasing the cell voltage. Under the best conditions, an MCDI unit with a 20 wt% Mn_2O_3 composite AEM and a bipolar membrane facilitated high phosphate removal efficiency of ≥ 31.8 % and a phosphate over chloride selectivity of 1.1 while showing stability for at least 30 cycles. To help understand how manganese oxide particles boost AEM selectivity, static electronic structure calculations were performed, and they revelated that hydrogen phosphate absorption on Mn_2O_3 composite AEM was 314 kcal/mol more exothermic than that on pristine AEM while chloride adsorption

on Mn_2O_3 composite AEM was 2.2 kcal/mol less exothermic than that on a pristine AEM. Overall, this work presents an effective strategy for selectively removing phosphate from model wastewater solutions and the mechanistic understanding that governs ion selectivity in composite ion-exchange membranes used in MCDI.

Keywords: phosphate removal, ion selectivity, manganese oxide, composite anion exchange membranes, bipolar membranes, membrane capacitive deionization

INTRODUCTION

Phosphorus is an essential nutrient for life, but its excessive discharge into water bodies causes serious eutrophication, threatening ecosystems of water bodies.[1, 2] Therefore, removing phosphate from wastewater is essential to protecting water resources. The most common approach for removing phosphate from wastewater solutions include chemical precipitation[3-5], adsorption[6-9], and biological methods[10, 11]. While chemical precipitation is a quick and efficient means for removing phosphorus from water[3], this process generates a significant amount of chemical waste such as sludge, raises the pH of treated water, and consumes a substantial amount of energy. Additionally, the resulting phosphorus crystals may be contaminated with other ions, making reuse difficult. The biological method for capturing phosphate utilizes specialized bacteria under alternating anaerobic and aerobic conditions leading to lower energy consumption and efficient phosphorus removal through the formation of polyphosphate sludge.[12-14] However, environmental factors like temperature and pH can significantly impact its effectiveness, and it is difficult to scale up the biological method. The adsorption method leverages a particle's affinity towards phosphate ions for selective removal from water.[6, 7, 15] However, this technique necessitates chemicals for regenerating the adsorbent.

Capacitive deionization (CDI) is an electrochemical process that is effective for desalinating brackish water.[16-19] It captures and stores ions in the electrochemical double layer (EDL) of the porous electrodes during the charge process. Once the electrode is saturated (or approaching saturation), the absorbed ions in the EDL are desorbed and released back into the process stream.[20, 21] This step is known as the discharge process. An alternative platform to CDI is membrane capacitive deionization (MCDI). This variant features two ion-exchange membranes (one anion exchange membrane (AEM) and the other a cation exchange membrane

(CEM)) that are placed adjacent to the electrodes to prevent co-ion adsorption leading to greater charge efficiency.[22-25] Conventional CDI and MCDI platforms are effective for desalination as they remove all the types of ions in the water stream. However, if one is interested in targeting a specific ion, such as a bad actor or valuable species, conventional MCDI and CDI are unable to discriminate between ions – especially those of the same valence and hydration radius.

This work is primarily motivated by removing phosphate from model wastewater solutions. Previous researchers have modified electrode materials to achieve selective phosphate removal via CDI or MCDI.[20, 26-28] Transition metals such as Fe[7, 8, 29, 30], Mn[6, 8, 9], Zr[26, 31] and Cu[29] form inner-sphere complexes with phosphorous thereby increasing the absorption and selectivity of phosphate over competing ions. For instance, Zhang et al.[26] reported an organic–inorganic composite material (ZnZr-COOH/CNT) as an electrode in CDI, which exhibited a high adsorption capacity of phosphate under a low feed concentration of phosphate (~10 mg/L). Zhang et al.[30] coated Fe_3O_4 on the surface of active carbon electrodes and these electrodes exhibited a phosphorus to chloride (P/Cl) selectivity of 1.42 at low current density values (3.4 A m^{-2}). Hong et al.[20] showed that layered double hydroxide/reduced graphene oxide (LDH/rGO) composite electrodes reached a high P/Cl selectivity of 6.1. They attributed this outcome to an inner-sphere complexation of a ligand exchange reaction between phosphate ions and polarized LDH/rGO. Another strategy to improve phosphate selectivity involves the use of ion exchange layer coatings on the electrodes. Shen et al.[27] reported an anion exchange resin-coated activated carbon electrode that improved P/Cl to 0.56. The baseline control showed a P/Cl of 0.25 with uncoated activated carbon electrode. Wang et al.[28] designed a covalent organic framework-membrane coating electrode (COF-MCE) for CDI, which exhibited a high P/Cl selectivity of 3.62. The COF-MCDI contained a positive surface charge and other moieties that promoted hydrogen bonding interactions to facilitate selective phosphorus removal. The COF's high specific surface area also assisted with phosphate removal efficiency. Several research groups have explored flow-electrode capacitive deionization (FCDI)[30, 32, 33] for selective phosphate removal. Xu and Yu et al. reported a P/Cl > 2 in FCDI while also showing a relative low specific energy consumption (SEC) value of 27.8 kWh/kg of P.[33] In addition to electrode modification, membrane modification is another strategy for improving phosphate selectivity. Iddya et al.[34] prepared a composite CEM containing hydrous magnesium oxide nanoparticles and this CEM gave a high P/Cl selectivity of 20 through an outer-sphere complexation–diffusion pathway. However, this membrane modification strategy was not evaluated in an electrochemical

separation platform such as MCDI. Furthermore, the CEM will repel most dissociated phosphate anions via Donnan exclusion and will have poor phosphate removal efficiency if deployed in an electrochemical separation platform. **Table S1** summarizes the experimental conditions and performance attributes of state-of-the-art phosphate removal selectivity.

This work reports a manganese oxide composite AEM that improves phosphate selectivity and phosphate removal when deployed in MCDI. We systematically investigated several critical factors that govern the removal efficiency and selectivity of phosphate. These factors include charge mode (i.e., constant current versus constant voltage), solution pH, applied voltage amount, and the manganese oxide content in AEM. We found that phosphate selectivity is enhanced when operating the MCDI with a composite AEM consisting of 20 wt% manganese oxide unit under constant voltage mode and applying a relatively low cell voltage, and making the process stream alkaline. Notably, we observed that increasing the cell voltage led to a larger removal efficiency of phosphate but at the expense of phosphate selectivity over chloride. We used static electronic structure calculations to understand the mechanism of selective phosphate capture by Mn_2O_3 composite AEMs. The calculation results reveal that hydrogen phosphate (HPO_4^{2-}) absorption on Mn_2O_3 composite AEM was 314 kcal/mol more exothermic than that on pristine AEM while Cl^- adsorption on Mn_2O_3 composite AEM was 2.2 kcal/mol less exothermic than that on pristine AEM. Finally, a MCDI unit featuring a 20 wt% manganese oxide composite AEM and a bipolar membrane (for tuning the pH to an alkaline value) demonstrated ≥ 31.8% phosphate removal efficiency and a P/Cl selectivity of 1.1 over 30 cycles (feed: 10 mM NaCl + 1 mM NaH_2PO_4; single pass with a 25 cm^2_{geo} active area). Overall, new materials and tuned MCDI operating parameters were combined for selective phosphate removal from sodium chloride-sodium dihydrogen phosphate aqueous salt mixtures. Furthermore, density functional theory (DFT) calculations are brought to bear in revealing the molecular underpinnings that govern ion-selectivity with composite ion-exchange membranes.

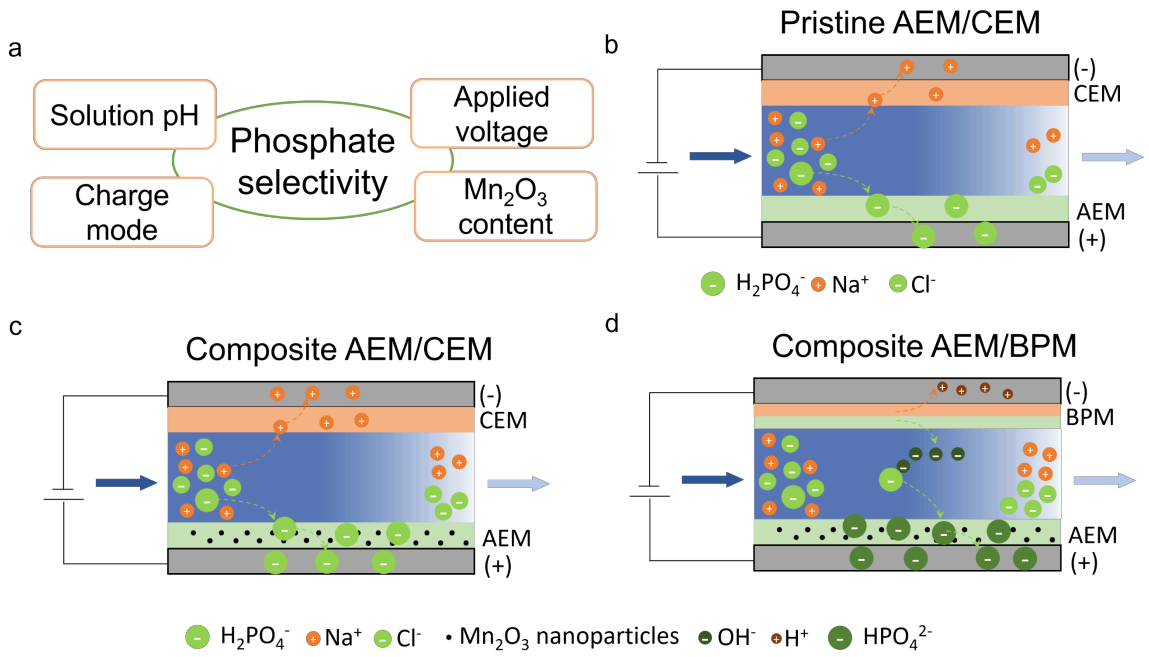

Figure 1. (a) Critical factors affecting phosphate selectivity in membrane capacitive deionization (MCDI) experiments. Schematic of flow-by MCDI for phosphate removal from aqueous salt mixture feeds with different membrane configurations: (b) pristine anion exchange membrane (AEM) with a pristine cation exchange membrane (CEM), (c) Mn_2O_3 composite AEM with a pristine CEM and (d) Mn_2O_3 composite AEM with a bipolar membrane (BPM).

MATERIALS AND METHODS

Materials

N,N'-dimethylacetamide (DMAc), N-Methyl-2-pyrrolidone (NMP), trifluoromethanesulfonic acid, sodium chloride (NaCl), tetrahydrofuran (THF), monosodium dihydrogen phosphate (NaH_2PO_4), sodium nitrate ($NaNO_3$), silver nitrate ($AgNO_3$) and potassium chromate (K_2CrO_4) were received from Sigma Aldrich. Udel poly(arylene ether) sulfone (PSf) was received from Acros Organics. Sodium 3-(trimethylsilyl)-1-propanesulfonate (DSS) was attained from TCI America. Chloroform and methanol were sourced from VWR. 7-Bromo-1,1,1-trifluorohexane-2-one and m-terphenyl were purchased from SynQuest Inc. All chemicals listed above were used as is. Manganese oxide particles water suspension was received from US Research Nanomaterials, Inc. Carbon cloth was purchased from Kuraray and was activated by treating with 1 M nitric acid at 85 °C and used as carbon electrodes. Commercially available bipolar membranes from Fumatech (FUMASEP-FBM) were purchased from the Fuel Cell Store.

Synthesis of the AEM polymer

The synthesis of pol(phenyl alkylene) anion exchange ionomers to fabricate pristine AEMs was described in our previous work[35]. This ionomer material was used in the preparation of composite AEMs with manganese oxide particles. The synthesis is briefly described here: m-terphenyl and 7-bromo-1,1,1-trifluorohexane-2-one were mixed and added to a 3-neck, 250 mL round bottom flask equipped with a nitrogen inlet, magnetic stirrer, and dropping funnel. After purging the flask with nitrogen, anhydrous DCM was added, and the mixture was cooled to 0 °C using an ice bath. Trifluoromethanesulfonic acid was then added dropwise to the flask, followed by stirring the contents within the flask for 16 hours. During this time period, the flak was allowed to warm up to room temperature. The resulting solution was then poured into methanol to precipitate the ionomer polymer. The polymer was washed with methanol and dried after filtration. The collected brominated poly(terphenylene alkylene) (mTPBr) was then dissolved in THF, precipitated in methanol, filtered, and dried. This latter step is performed to remove impurities from the polymer. In a separate reaction, 15g mTPBr was dissolved in 150 mL DMAc and 34 mL trimethylamine (33 w/w% in EtOH) was added to convert the bromo-alkyl groups to quaternary alkyl trimethyl ammonium groups. This reaction occurred over 24 hours at room temperature while stirring in a round bottom flask (250 mL). The ionomer material was collected from the flask by precipitating it in THF. After filtration and drying, the resulting anion exchange ionomer was obtained for fabricating AEMs.

Synthesis of CEM polymer

Sulfonated polysulfone (sPSf) was prepared by following the procedure of Martos et al.[36] Briefly, polysulfone (PSf) was dissolved in chloroform, treated with trimethylsilyl chlorosulfonate to form a silyl sulfonate PSf intermediate. Sodium methoxide was added to cleave the silyl sulfonate, yielding the final sPSf ionomer. The polymer was precipitated in isopropyl alcohol, washed with methanol, and rinsed with DI water. The obtained solid ionomer was dried at 110 °C.

Preparation of pristine AEMs and CEMs and composite AEMs

Pristine AEMs and CEMs were prepared by drop casting dissolved ionomer solutions on a clean and levelled glass plate. The ionomer solution for pristine AEMs was 5 wt% polymer in NMP solvent. The solvent was evaporated from the drop casted anion exchange ionomer at 70 °C overnight. Afterwards, the dried membrane was removed from the glass plate with the assistance of deionized water. The pristine CEMs were prepared by drop casting 5 wt% of the ionomer in DMAc solvent on to the glass plate in an oven and the solvent was evaporated from

the CEM at 115 °C overnight. The CEM was removed from the glass plate with the assistance of DI water.

To prepare composite AEMs, manganese oxide particles dispersed in water were dried in the oven at 70 °C overnight to collect manganese oxide powder. The manganese oxide powder was characterized by XRD as shown in **Figure S1**. Based on the anion exchange ionomer mass, we added 5 wt%, 10 wt% and 20 wt% Mn_2O_3 powder to the dissolved ionomer solution (5 wt% anion exchange ionomer in NMP) for making dispersions used in the fabrication of composite AEMs. The dispersion was drop casted on to glass plates in an oven, and the solvent was evaporated at 70 °C overnight. The obtained composite AEMs was removed from the glass plate with the assistance of DI water. All membranes extracted from the glass plate were stored in DI water before using in MCDI experiments or characterizing them. The thickness values of the membranes were recorded using a digital micrometer. For all the membranes prepared, their thickness values were 40 ± 5 μm.

Water uptake measurements

The wet pristine AEM and composite AEMs in the phosphate form are weighed immediately after taking it from stored DI water and removing the surface water using Kimwipe. Then these membranes are dried at 60 °C in vacuum oven for 4-5 hours to obtain the dry forms of membranes. The water uptake is calculated according to the equation (1).

$$\text{Water uptake (\%)} = \frac{W_w - W_d}{W_d} \times 100 \qquad (1)$$

where W_w and W_d are the mass of wet and dry form of membranes.

Swelling ratio measurements

The same procedure for water uptake measurements given above was followed except Equation (2) below is used to calculate the swelling ratio of the membranes.

$$\text{Swelling ratio (\%)} = \frac{L_w - L_d}{l_d} \times 100 \qquad (2)$$

where L_w and L_d are the length of wet and dry form of membranes.

Membrane conductivity measurement

The ionic conductivity of pristine AEM and Mn_2O_3 composite AEMs in the phosphate form was measured in DI water using a four-point platinum cell[24] with poly(tetrafluoroethylene) (PTFE) housing. Electrochemical impedance spectroscopy (EIS) was collected in the frequency range of 100000−0.01 Hz with 10 data points per decade. The resistance was

determined by 0° phase angle data point in the EIS. The ionic conductivity of the membranes is calculated based on equation (3).

$$\kappa = \frac{d}{L \times W \times R} \quad (3)$$

Where d is the distance between the electrodes where the potential drop is measured, L is the membrane thickness, W is membrane width in the four-point probe, and R is the membrane resistance.

Ion-exchange capacity (IEC) measurement

The IEC values of pristine AEM and Mn_2O_3 composite AEMs were determined by Mohr titration. An AEM was soaked in 1 M NaCl solution for over 24 hours to exchange ions in the phosphate form to the chloride form. Then, the membranes were immersed in and rinsed with copious amounts of DI water (e.g., 6 to 8 times) to fully remove excess chloride counterions from the membrane. Afterwards, the membranes were dried at 70 °C for 6 hours in a vacuum oven to weigh the dry mass. The dry membranes were soaked in 0.1 M sodium nitrate solution for over 24 hours to convert ions from the chloride counteranion form to the nitrate counteranion form. Then the solution was transferred to a 100 mL beaker with 5 drops of potassium chromate as an indicator. Finally, the solution was titrated with 0.1 M silver nitrate solution and the IEC was calculated using equation (4).

$$IEC(mmol\ g^{-1}) = \frac{V_{silver\ nitrate} \times c_{silver\ nitrate}}{W_d} \quad (4)$$

Where $V_{silver\ nitrate}$ is the volume of added silver nitrate in the titration in mL, $c_{silver\ nitrate}$ is the concentration of silver nitrate solution.

MCDI experiments

The MCDI unit cell was assembled by placing a 5.2 cm x 5.2 cm AEM onto a 5 cm x 5 cm carbon cloth, followed by a cell spacer. Then a 5.2 cm x 5.2 cm CEM or BPM was placed onto the spacer before stacking another 5 cm x 5 cm carbon cloth. Note that the CEM side of the BPM faces the carbon cloth so that the AEM side of the BPM faces the process stream to hydroxide ions into the process stream for pH adjustment (**Figure 1d**). A feed solution of single 1200 ppm (20.5 mM) NaCl or 1200 ppm (10 mM) NaH_2PO_4 or a mixture of the two salts (1 mM NaH_2PO_4+ 10 mM NaCl) were pumped into the MCDI unit cell using a peristaltic pump at the rate of 3 mL min^{-1}. For single salt experiment, we used 0.8 mA cm^{-2} for discharge and charge. The charge time was 180 sec and discharge process were cutoff at 0 V. For mixture salts experiment with a CEM, we used 0.2 V, 0.5 V, 1.0 V and 1.5 V for charge process and -

0.5 V for discharge process. The charge and discharge time were 150 sec and 180 sec, respectively. For mixture salts experiments with a coupled BPM, we applied 1.2 V, 1.5 V, 2.0 V and 2.5 V for charge process and -0.5 V for discharge process. The charge and discharge time were 240 sec and 300 sec, respectively. The higher voltage applied in the variant using a BPM is used for water dissociation to generate hydroxide ions for the process streams while the protons migrate and are adsorbed into the negatively biased electrode.

Process stream and material characterization

Thermo-Fisher Ion-chromatography (IC) with a Dionex IonPac AS11-HC-4μm column was used to measure the concentration of chloride and phosphate in collected effluent samples from the MCDI unit during charge. The calibration curves of the IC measurements for both chloride and phosphate are given in **Figure S2**.

For XRD measurements, samples were placed on the flat side of a silicon zero background holder and diffraction data were collected from 10 to 80° 2θ using a Malvern Panalytical Empyrean® instrument fitted with a copper (Kα1=1.540598 Kα2 1.544426 Å) long-fine-focus X-ray tube operated at 45 kV and 40 mA. The incident beam path included iCore® optics fitted with a BBHD (Bragg Brentano HD)® optic with 0.03 radian Soller slits, a 14 mm primary and a 14 mm secondary mask, and a fixed 1/4° divergence slit. The diffracted beam path incorporated dCore® optics with a 1/4° fixed anti-scatter slit, and 0.04 radian Soller slits. A PIXcel3D® detector was used in scanning line (1D) mode with an active length of 3.347° 2θ. Data were collected with a nominal step size of 0.026° 2θ for 200 seconds. PHD lower and upper levels were set at 4.02 and 11.27 keV respectively. Phase ID was carried out using Jade® software (version 8.9) from Materials Data Inc. (MDI) and the International Centre for Diffraction Data (ICDD) PDF5® database.

Scanning electron microscopy (SEM) was performed using a Verios G4 model (Thermo-Scientific, Hillsboro OR) and the energy-dispersive X-ray spectroscopy (EDS) detector is the Xmax^N detector from Oxford Instruments, Concord, MA.

Equations used to assess phosphate removal efficiency and phosphate selectivity

The removal efficiency of specific ions (i.e., R_p or R_{Cl}) were calculated by equation (5):

$$Removal\ efficiency\ (\%) = \frac{C_0 - C_{eff}}{C_0} \times 100\% \qquad (5)$$

where C_{eff} and C_0 correspond to the effluent and feed stream salt concentrations, respectively. The selectivity of phosphate over chloride (P/Cl) was calculated using equation (6):

$$Selectivity = \frac{R_P}{R_{Cl}} \quad (6)$$

where R_p is the removal efficiency of phosphate and R_{Cl} is the removal efficiency of chloride.

Static Electronic Structure Calculations on Clusters

The potential energy surface for anion adsorption on representative clusters of the AEM and $MnPO_4 \cdot H_2O$ systems was calculated using the GAUSSIAN 16 program package[37]. Calculations were performed using the PBE functional[38-40] with the Grimme dispersion correction[41] along with the Becke and Johnson (BJ) rational damping function[42-44] (PBE-D3(BJ)). A mixed basis set of 6-311G*[45-47] (H, O, Cl, P) and Def2SVP[48, 49] (Mn) was used. The implicit water solvent was applied using the Integral Equation Formalism Polarizable Continuum Model (IEF-PCM)[50].

The potential energy surfaces of the adsorption process were obtained as a function of the distance between the ion (Cl^-, and P in HPO_4^{2-}) and the ammonium N in the AEM. For $MnPO_4 \cdot H_2O$, the $MnPO_4 \cdot H_2O$ (110) plane was built using the Avogadro software[51] based on the unit cell of the ideal crystal structure taken from Materials Project[52-66]. The cluster consists of four Mn, four P, eight H, and twenty O atoms. The relaxed energy scans were carried out by moving the anions along the direction of the normal vector of the (110) plane.

RESULTS AND DISCUSSION

Figure 1a conveys the parameters investigated in this work for phosphate removal from model sodium chloride and sodium dihydrogen phosphate (NaH_2PO_4) mixtures. **Figure 1b-d** depicts the three types of MCDI architectures investigated in this work: (1b) conventional MCDI that utilizes a pristine AEM and CEM, (1c) MCDI with a pristine CEM and a composite AEM featuring various concentrations of manganese oxide (Mn_2O_3) particles, and (1d) MCDI with a bipolar membrane and an optimized composite AEM with Mn_2O_3 particles.

Pristine and composite AEMs were prepared by drop casting anion exchange ionomer solutions with and without dispersed Mn_2O_3 particles. The composite AEMs contained Mn_2O_3 at different weight fractions (e.g., 5 wt%, 10 wt%, and 20 wt%). The pristine anion exchange membrane was synthesized via superacid-catalyzed Fridel-Crafts polycondensation of m-

Terphenyl and bromo-substituted ketone followed by quaternization reaction with trimethylamine[67]. The precursor polymer exhibited a molecular weight of Mn = 78000 g/mol (Đ = 2.3), which was determined by gel-permeation chromatography (GPC). The AEM structure was confirmed by ^{1}H NMR spectroscopy (**Figure S3**). **Figure 2a** shows pictures and electron micrographs of the pristine and composite AEMs. Additional electron micrographs and EDX images of pristine and composite AEMs are given in **Figures S2-S5**.

We then verified the manganese oxide state in composite AEMs before and after ion exchange in 1 M NaH_2PO_4 solution. We chose 20 wt% Mn_2O_3 composite AEM for this study because it contains the largest amount of Mn_2O_3. As shown in **Figure 2b**, all characteristic diffraction peaks in Mn_2O_3 composite AEMs agree well with the reference Mn_2O_3, indicating the Mn_2O_3 was successfully incorporated into the AEM. In contrast, the pristine AEM did not exhibit obvious diffraction peaks, confirming the pristine AEM is an amorphous material. **Figure 2c** presents the XRD pattern for the 20 wt% Mn_2O_3 composite AEMs after ion-exchange in 1 M NaH_2PO_4 for 3 days. The XRD data in **Figures 2b** and **2c** demonstrate that the Mn_2O_3 in the composite AEMs was converted to $MnPO_4{\cdot}H_2O$. This conversion is attributed to the reaction between transition metal oxide (Mn_2O_3) and weak acid (NaH_2PO_4). After ion exchange, converted $MnPO_4{\cdot}H_2O$ exhibits flake-like morphology in contrast to nanoparticles of Mn_2O_3 as shown in **Figure S4**. The uniform distribution of phosphorous suggests that ion exchange from chloride to phosphate was completed for all membranes and $MnPO_4{\cdot}H_2O$ was formed from the Mn_2O_3 in composite AEMs (**Figure S5-S8**).

Ion-exchange membranes with low water uptake, low swelling ratio, high conductivity and high ion-exchange capacity (IEC) are desired for most electrochemical processes, including MCDI. The low water uptake and swelling signals robust mechanical properties when interfaced with an aqueous solution. Ion-exchange membranes with large water uptake values leads to excessive swelling, poor mechanical properties, and poor contact with electrode materials. High ionic conductivity is important for reducing the area specific resistance within the cell and the ohmic overpotential. **Table 1** gives the key characteristics of pristine and Mn_2O_3 composite AEMs, including water uptake, membrane conductivity, swelling ratio and ion-exchange capacity. Both types of AEMs exhibited water uptake values of ~20% and swelling ratio of ~9%, which is acceptable for MCDI and comparable to commercial AEM variants from Fumasep (15% water uptake and 4% swelling ratio)[35]. Furthermore, the Mn_2O_3 composite

AEMs had similar water uptake and swelling ratio values to pristine AEM, indicating incorporation of Mn_2O_3 into the AEM matrix did not affect the membrane's water uptake or swelling ratio. The membrane conductivity decreases with the increase of Mn_2O_3 content due to $MnPO_4 \cdot H_2O$ not containing any tethered charge groups that facilitate ionic conductivity. For instance, the 20 wt% Mn_2O_3 composite AEM exhibits a conductivity of 6.4 mS cm^{-1} while the pristine AEM has a conductivity of 9.9 mS cm^{-1} as measured in DI water at room temperature. The pristine AEM exhibited a high IEC of 2.0 meq g^{-1}. With the increase of Mn_2O_3 content in the AEM, the IEC of Mn_2O_3 composite AEM decreased because the $MnPO_4 \cdot H_2O$ does not contain any tethered, dissociated cation groups. The 5 wt%, 10 wt% and 20 wt% Mn_2O_3 composite AEMs show an IEC of 1.9, 1.8 and 1.6 meq g^{-1}, respectively.

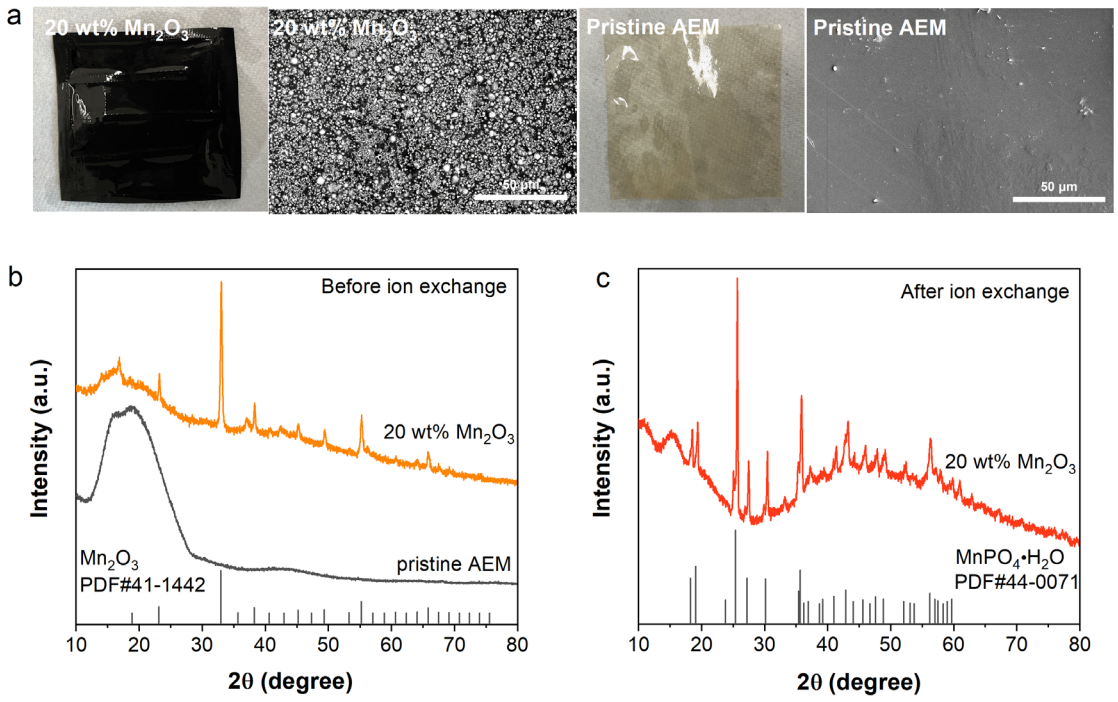

Figure 2. (a) Photo and SEM images of 20 wt% Mn_2O_3 composite AEM and pristine AEM. XRD patterns of (b) pristine AEM and 20 wt% Mn_2O_3 composite AEM before ion exchange and (c) 20 wt% Mn_2O_3 composite AEM after ion exchange in 1 M NaH_2PO_4 solution.

Table 1. Ion-exchange capacity, water uptake, swelling ratio, and ionic conductivity of pristine and composite AEMs

Membrane type	Ion-exchange capacity (meq g^{-1})	Water uptake (%)	Swelling ratio (%)	Ionic conductivity in DI water (mS cm^{-1})
Pristine AEM	2.0	21.5	9.7	9.9
5 wt% Mn_2O_3 composite AEM	1.9	21.5	9.4	7.5
10 wt% Mn_2O_3 composite AEM	1.8	20.5	7.8	7.8
20 wt% Mn_2O_3 composite AEM	1.6	20.8	8.6	6.4

We first investigated the Mn_2O_3 composite AEM for ion removal in MCDI with a single salt aqueous solution feed (e.g., either 1200 ppm NaCl in DI water or 1200 ppm NaH_2PO_4 in DI water). These experiments tested four types of AEMs: pristine AEM (i.e., 0% Mn_2O_3) and composite AEMs that had 5 wt% Mn_2O_3, 10 wt% Mn_2O_3 and 20 wt% Mn_2O_3. These experiments were performed under constant current charge and discharge (0.8 mA cm^{-2}). The current density value was maximized for increased salt removal while making sure the cell voltage did not exceed 1.5 V to prevent the occurrence of parasitic reactions like carbon oxidation[24, 68]. As shown in **Figure 3a**, the phosphate concentration after charge with 10 wt% and 20 wt% Mn_2O_3 composite AEMs are 954 ppm and 963 ppm, respectively. These values are lower than the pristine AEM case – which showed a phosphate concentration of 1022 ppm after charge. This observation demonstrates that Mn_2O_3 composite AEMs promote phosphate uptake and removal. Regarding deionization experiments for chloride removal, the Mn_2O_3 composite AEM showed a slightly higher chloride concentration after charge compared to pristine AEM (954 ppm for 10 wt % Mn_2O_3 and 951 ppm for 20 wt% Mn_2O_3 composite AEM compared to 932 ppm for pristine AEM). The voltage versus time profile under constant current charge and discharge was about the same for pristine and composite AEMs for a given single salt feed solution (**Figure S9**). The single salt absorption/desorption result indicate that Mn_2O_3 composite AEMs improve phosphate removal over pristine AEMs without increasing the removal of competing chloride ions.

In the experiments with salt mixtures (10 mM NaCl+ 1 mM NaH_2PO_4), we first examined the charge mode (either constant voltage charge (CVC) or constant current charge (CCC)) on phosphate removal efficiency and P/Cl selectivity. For CVC, we set the cell voltage to 1.5 V. Exceeding this cell voltage may spur water electrolysis or electrode corrosion. CCC was performed at 0.8 mA cm^{-2} - the same current density value mentioned in the previous section. The CCC mode of 0.8 mA cm^{-2} was used to compare with the CVC mode of 1.5 V because 1.5 V constant charge produces a steady current density of 0.8 mA cm^{-2} as shown in **Figure S10**. **Figures 3c** and **3d** present the phosphate removal efficiency and P/Cl selectivity values for CCC mode and CVC mode with pristine and composite AEMs in the MCDI unit. These results demonstrate higher phosphate removal efficiency and P/Cl selectivity values for CVC mode than CCC mode under three different AEMs. For instance, 10 wt% Mn_2O_3 AEM exhibited a phosphate removal efficiency of 33.6% and a P/Cl selectivity of 0.66 under CVC mode, while CCC mode showed a phosphate selectivity of 13.8% and a P/Cl selectivity of 0.46. Other literature repots have also demonstrated that CVC facilitates more salt adsorption compared to CCC mode[69, 70]. However, this effect may be dependent on many factors such as feeding solution concentration, effluent concentration and effluent volume[71] and it is prudent not to make too broad claims stating that CVC is more effective under all conditions. In our experiments, we found CVC mode to be more efficient than CCC mode for phosphate selectivity. We attribute these results to the smaller effluent volume (7.5 mL) and lower phosphate concentration in the effluent[71]. As reported by Lin and Wang[71], CVC mode outperforms CCC mode under smaller solution volume (e.g. 50 mL) and lower effluent concentration of 10.4 mM with the 20 mM feeding solution.

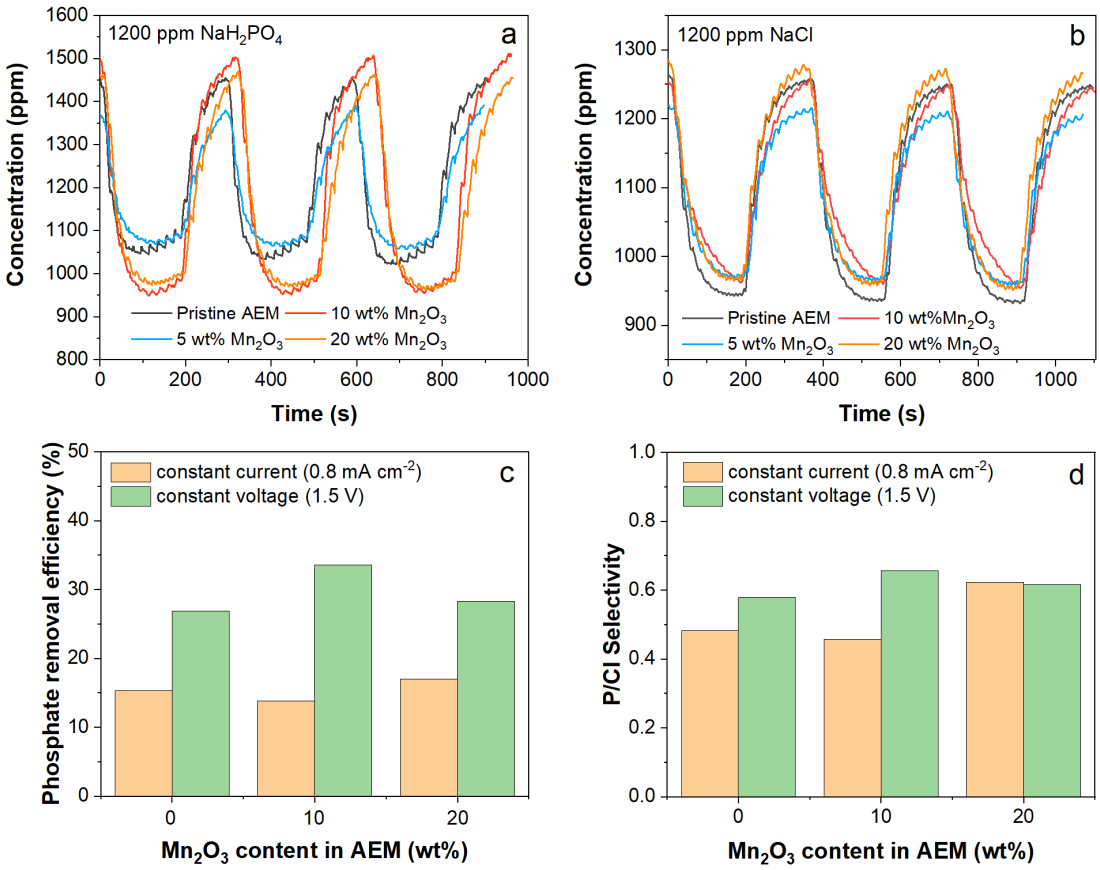

Figure 3. Concentration changes during discharge-charge tests with single salt feeds for different AEMs in MCDI with (a) 1200 ppm (10 mM) NaH_2PO_4 and (b) 1200 ppm (20.5 mM) NaCl. (c) Phosphate removal efficiency comparison and (d) P/Cl selectivity comparison for salt mixture feeds in MCDI operated under constant current charge (CCC) mode and constant voltage charge (CVC) mode with different AEMs.

The second set of experiments investigated the pH effect on phosphate selectivity with pristine and composite AEMs in MCDI. As shown in equations (7)-(9)[27, 28, 32], a strong acid environment (pH < 2.15) leads to H_3PO_4 being the major species. pH adjusting the stream to over 7.20 deprotonates H_3PO_4 to $H_2PO_4^-$. Making the process stream more alkaline (7.20<pH<12.35) yields HPO_4^{2-} - a divalent ion. pH adjusting the stream to over 12.35 leads to the trivalent PO_4^{3-} anion. We postulated that ionizing the phosphorus species to $H_2PO_4^-$ and HPO_4^{2-} via pH adjustment would enhance phosphate removal efficiency and selectivity. The ionized species are more susceptible to electric field driving forces during deionization.

$$H_3PO_4 \leftrightarrow H_2PO_4^- + H^+ \quad pK_{a1} = 2.15 \quad (7)$$

$$H_2PO_4^- \leftrightarrow HPO_4^{2-} + H^+ \quad pK_{a2} = 7.20 \quad (8)$$

$$HPO_4^{2-} \leftrightarrow PO_4^{3-} + H^+ \quad pK_{a3} = 12.35 \quad (9)$$

Figures 4a-d shows the removal efficiency of phosphate and P/Cl selectivity under different pH values for the feed solution (10 mM NaCl +1 mM NaH_2PO_4). We measured the pH of the feed solution (10 mM NaCl +1 mM NaH_2PO_4), obtaining a value of 5.23. Upon the addition of 1 mM NaOH to the feed solution, the solution pH was observed to be 8.63. These two pH values (5.23 and 8.63) were evaluated because the first pH value (5.23) yields the monovalent $H_2PO_4^-$ species while the other pH value (8.63) ensures the ionization in the form of the divalent HPO_4^{2-} species. We chose not to raise the pH further because highly alkaline solutions can be detrimental from a post-processing (environmental) perspective. The data in **Figures 4a-d** convey that phosphate selectivity improved with a more alkaline pH environment (i.e., pH = 8.63). For example, the P/Cl selectivity increased from 0.57 for pH 5.23 to 0.65 for pH 8.63 for the pristine AEM in the MCDI unit (**Figure 4b**). Implementing the 20 wt% Mn_2O_3 composite AEM into the MCDI unit led to a P/Cl selectivity of 0.73 at pH 8.63 (**Figure 4d**). The P/Cl selectivity for this AEM in MCDI at pH 5.23 was 0.62.

The greater P/Cl selectivity observed with pH 8.63 is attributed to divalent ions having higher ionic conductivity than monovalent ions provided the ionic mobility values between the two species are not that different. Ionic conductivity scales to the square value of the ion's valence[72]. Furthermore, the higher P/Cl selectivity at pH 8.63 could arise from the stronger electrostatic attraction between divalent HPO_4^{2-} ions and the carbon electrode surface when compared to the monovalent $H_2PO_4^-$ ions and carbon electrode surface[27, 28, 73]. The electrosorption capacity of carbon electrodes is a function of the with ionic charge in the solution[27, 74]. **Figure S11** also shows that 5 wt% and 10 wt% Mn_2O_3 composite AEMs exhibited a higher P/Cl selectivity at pH 8.63 versus pH 5.23.

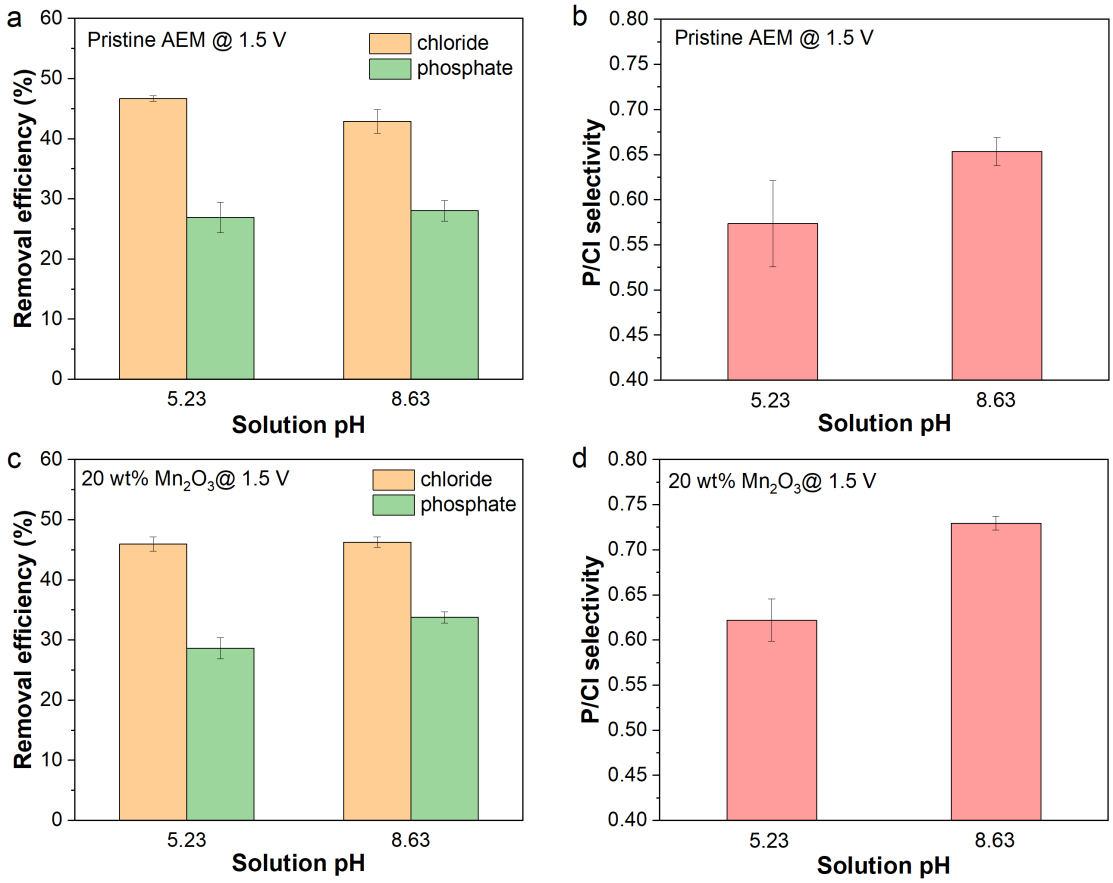

Figure 4. The removal efficiency of phosphate and chloride of (a) pristine AEM and (c) 20 wt% Mn_2O_3 composite AEM at 1.5 V under different pH conditions. Corresponding P/Cl selectivity of (b) pristine AEM and (d) 20 wt% Mn_2O_3 composite AEM.

The next experiments studied phosphate removal efficiency and P/Cl selectivity as a function of the applied cell voltage. Four different cell voltages were applied: 0.2 V, 0.5 V and 1.0 V and 1.5 V. As stated before, we set an upper limit to 1.5 V on the unit (when not using a BPM) to mitigate water electrolysis and carbon corrosion – which both represent parasitic reactions that compromise current efficiency. These experiments were performed with salt mixtures (10 mM NaCl +1 mM NaH_2PO_4) at pH 8.63 (adjusted externally by adding 1 mM NaOH) based upon the previous section's results. Increasing the cell voltage led to larger phosphate removal efficiency values for all AEMs studied (i.e., the pristine AEM and composite AEMs with different Mn_2O_3 wt% values; **Figure 5a-d**). For example, 20 wt% Mn_2O_3 composite AEM exhibited a phosphate removal efficiency of 13.7%, 20.7%, 29.1% and 33.8% at 0.2 V, 0.5 V, 1.0 V and 1.5 V, respectively. The larger cell voltage provided a stronger driving force for phosphate removal from the process stream, but this greater removal rate came at the expense of using more energy – manifested in the larger voltage values. At the same time, the P/Cl

selectivity decreased with the increase of applied voltage. Chloride ion removal efficiency displayed a stronger response to increasing cell voltage and electric field strength compared to phosphate anions. For example, 10 wt% Mn_2O_3 composite AEM showed a P/Cl selectivity of 0.85, 0.79, 0.74 and 0.69 at 0.2 V, 0.5 V, 1.0 V and 1.5 V, respectively. 20 wt% Mn_2O_3 composite AEM showed a P/Cl selectivity of 0.90, 0.80, 0.75 and 0.73 at 0.2 V, 0.5 V, 1.0 V and 1.5 V, respectively. The ionic mobility of chloride is higher than phosphate anions and this accounts why chloride ions removal efficiency increases more with larger cell voltages resulting in lower P/Cl selectivity values.

The applied cell voltage studies indicate that the cell will need to be operated at lower voltages to promote P/Cl selectivity values, but this comes at the expense of lower current density values and lower phosphate removal efficiency. This will require a larger stack and membrane area for given phosphate removal duty.

Next, we evaluated the Mn_2O_3 content in the composite AEMs on the ion removal efficiency and P/Cl selectivity at pH 8.63 of the feed solution. The Mn_2O_3 content varied from 0 to 20 wt%. Increasing the Mn_2O_3 content in the composite AEM boosted the P/Cl selectivity under a wide voltage window ranging from 0.2 V to 1.5 V. The removal efficiency and P/Cl selectivity results under 0.5 V and 1.5 V are shown in **Figure 5e-f** and the results under 0.2 V and 1.0 V are shown in **Figure S12**. The pristine AEM, 5 wt% Mn_2O_3, 10 wt% Mn_2O_3 and 20 wt% Mn_2O_3 composite AEM exhibited a P/Cl selectivity of 0.65, 0.72, 0.79 and 0.80 under 0.5 V (**Figure 5e**). The P/Cl selectivity of 20 wt% Mn_2O_3 composite AEM increased by 23% compared to pristine AEM at 0.5 V. At a higher voltage of 1.5 V, the pristine AEM, 5 wt% Mn_2O_3, 10 wt% Mn_2O_3 and 20 wt% Mn_2O_3 composite AEM exhibited a P/Cl selectivity of 0.65, 0.68, 0.69 and 0.73 (i.e., a 12% increase in P/Cl selectivity was achieved for 20 wt% Mn_2O_3 composite AEM over a pristine AEM at 1.5 V). These results clearly demonstrate that incorporation of Mn_2O_3 particles into AEMs enhance phosphate selectivity in MCDI units.

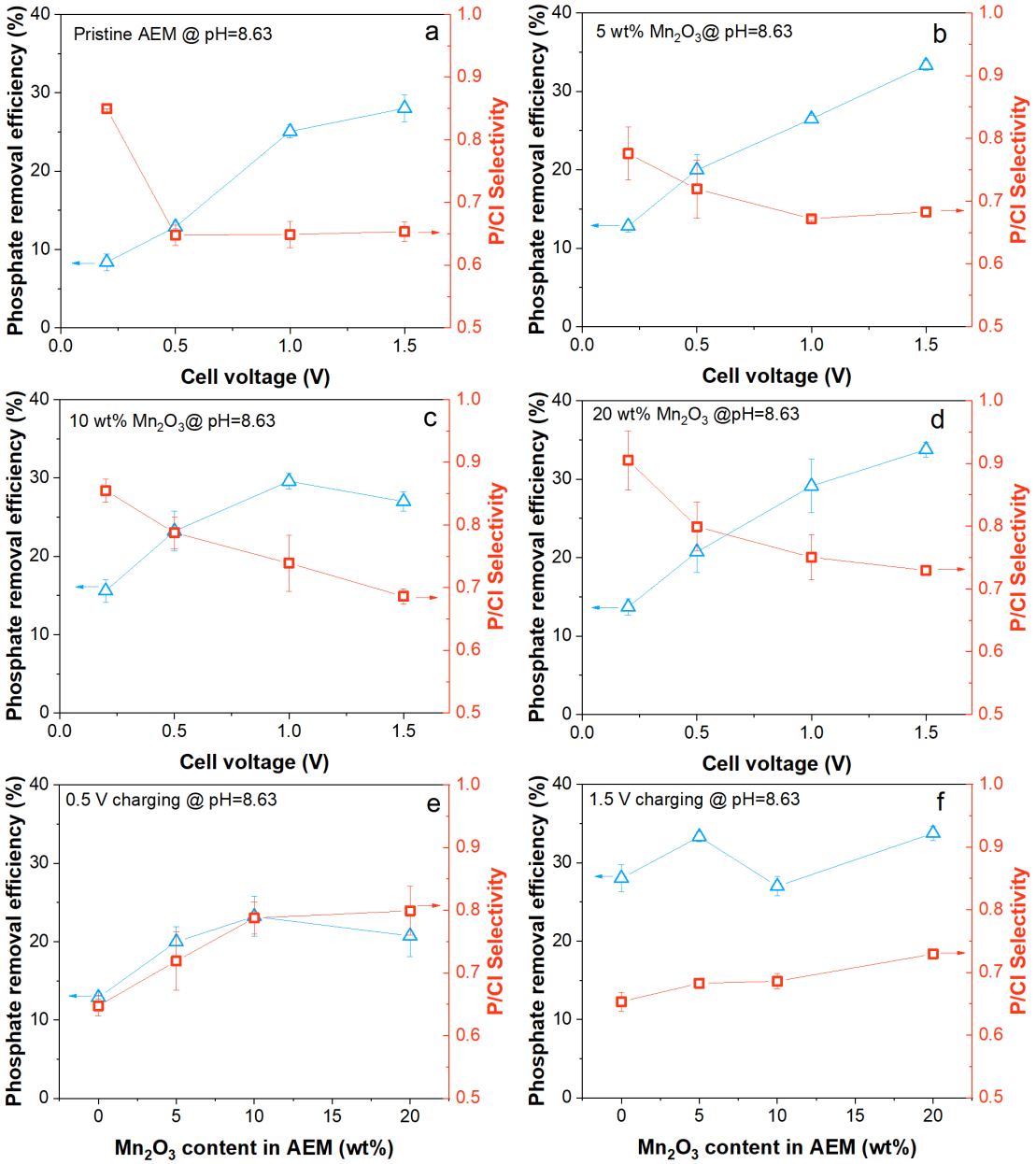

Figure 5. Phosphate removal efficiency and P/Cl selectivity at pH 8.63 for (a) pristine AEM, (b) 5 wt% Mn_2O_3, (c) 10 wt% Mn_2O_3 and (d) 20 wt% Mn_2O_3 under different MCDI cell voltage values. Phosphate removal efficiency and P/Cl selectivity at pH 8.63 at (e) 0.5 V and (f) 1.5 V with different Mn_2O_3 concentrations in composite AEMs.

The calculated energy diagrams of the anion adsorption on the AEM and the $MnPO_4 \cdot H_2O$ are shown in **Figure 6**. For the case of the adsorption of Cl^- on the AEM (**Figure 6a**), the Cl^- forms hydrogen bonds with the three CH_3- groups on the quaternary ammonium moiety in the AEM, resulting in a decrease in the total potential energy by 4 kcal/mol compared to when the ions are separated. When HPO_4^{2-} adsorbs on the AEM, as shown in **Figure 6b**, three hydrogen bonds

are formed between the O atoms in the HPO_4^{2-} ion and the C atoms in the quaternary ammonium CH_3- groups in the AEM, decreasing the total free energy by 16 kcal/mol comparing with the separated ions. For adsorption of Cl^- on the $MnPO_4 \cdot H_2O$ (**Figure 6c**), the surface Mn shifts inward within the $MnPO_4 \cdot H_2O$ crystal. Meanwhile its adjacent O atom, initially pointing away from the surface, reorients so that Mn-O bond becomes parallel to the interface plane; thus the surface Mn atom becomes exposed to the Cl^- in water solution. This transition state corresponds to an energy barrier of 15 kcal/mol comparing with the relaxed surface, and there is a subsequent decrease in the potential energy of 16.8 kcal/mol for the final adsorption state compared to the transition state. For HPO_4^{2-} and $MnPO_4 \cdot H_2O$ (**Figure 6d**), one O in HPO_4^{2-} forms a bond with the surface Mn, another O in HPO_4^{2-} coordinates with the Mn atom in the second layer in the cluster, and the OH group in the HPO_4^{2-} forms hydrogen bond with O atoms in $MnPO_4 \cdot H_2O$, decreasing the potential energy by 330 kcal/mol. The overall energy change associated with the anion propensity for the substrate is equivalent to the calculated adsorption energy, representing the amount of energy released when the anion adsorbs on the surface, minus the hydration energy of that specific anion. The hydration energy is the amount of energy released when the ion undergoes hydration in bulk aqueous solution. The hydration energy of a specific anion remains constant when comparing its behaviour at the surface of $MnPO_4 \cdot H_2O$ to that on the AEM analogue. As a result, for HPO_4^{2-}, adsorption on the $MnPO_4 \cdot H_2O$ cluster is 314 kcal/mol more exothermic than adsorption on the AEM analogue. Conversely, Cl^-, adsorption on the $MnPO_4 \cdot H_2O$ cluster is 2.2 kcal/mol less exothermic than on the AEM analogue, with an additional energy barrier of 15 kcal/mol. Consequently, the $MnPO_4 \cdot H_2O$ cluster exhibits significant enhancements in the adsorption of HPO_4^{2-}, and a reduction in the adsorption of Cl^-, thereby promoting the selectivity of HPO_4^{2-} over Cl^- in composite AEMs – as observed in MCDI experiments.

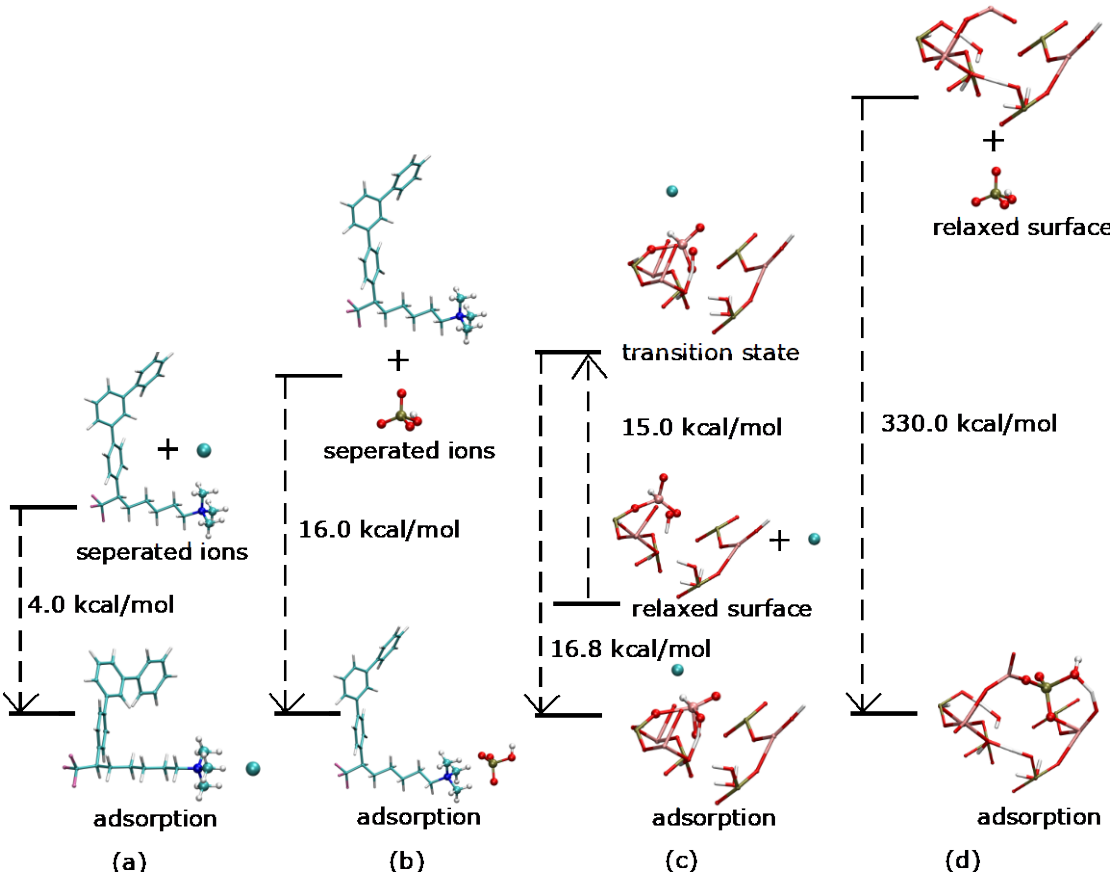

Figure 6. Comparison and relative potential energies of the four different adsorption processes. (a) Cl^- on the AEM; (b) HPO_4^{2-} on the AEM; (c) Cl^- on the $MnPO_4 \cdot H_2O$ cluster; (d) HPO_4^{2-} on the $MnPO_4 \cdot H_2O$ cluster. The white, green, pink, and blue in the AEM represent H, C, F, and N respectively. The white, red, pink, and tan in $MnPO_4 \cdot H_2O$ cluster represent H, O, Mn, and P, respectively.

The final experiments examined phosphate removal efficiency and P/Cl selectivity in MCDI featuring a 20 wt% Mn_2O_3 composite AEM and a bipolar membrane (BPM). Implementing a BPM into the MCDI unit allows for in-situ pH adjustment of the process stream without the addition of adding acid or base to the process stream before feeding into the MCDI unit[23]. This simplifies the electrochemical separation unit and makes it more amenable for distributed separations. Plus, sodium hydroxide hails from the energy intensive chlor-alkali process. Lienhard and co-workers[75] have reported that BPM electrodialysis has a lower theoretical energy use for generating NaOH when compared to chlor-alkali. As shown in our previous work[23], substituting the CEM with a BPM in MCDI and placing the cation exchange layer side of the BPM near the negative electrode during deionization leads to an alkaline process stream. It is important to note that a higher cell voltage needs to be applied because energy is needed to dissociate water at the bipolar junction interface to generate protons and hydroxide ions.[23,

[76]. The thermodynamic minimum voltage needed for water dissociation is 0.83 V. The commercial Fumasep BPM deployed in this configuration has an onset potential for water dissociation of ~1 V[77]. MCDI experiments with a BPM were performed at cell voltage values of 1.2 V, 1.5 V, and 2.0 V, and 2.5 V. The MCDI unit schematic with a composite AEM and BPM is given in **Figure 1d**. MCDI experiments with a BPM used a composite AEM with 20 wt% Mn_2O_3 because this AEM had the highest P/Cl selectivity of the composite AEMs tested.

Figure 7a presents the phosphate removal efficiency and P/Cl selectivity for a MCDI unit with a composite AEM and a BPM. The feed solution was 10 mM NaCl+ 1 mM NaH_2PO_4 and the feed solution was not pretreated with a base externally for this set of experiments. The initial feed solution pH was 5.2. Similar to the results in the previous section on changing the cell voltage, larger cell voltage values in BPM MCDI with composite AEMs increased phosphate removal efficiency values. For example, the phosphate removal efficiency improved from 15.8% at 1.2 V to 42.9% at 2.5 V. Interestingly, the P/Cl selectivity first increased with increasing cell voltage then gradually decreased with further increases in cell voltage. The highest P/Cl selectivity is 1.1 at 1.5 V with a phosphate removal efficiency of 30.8%. The P/Cl selectivity and phosphate removal efficiency are 1.0 and 39.2% at 2.0 V and 0.9 and 42.9% at 2.5 V, respectively. This result also indicates a trade-off between the P/Cl selectivity and phosphate removal efficiency when applying greater voltages (i.e., 2.5 V). It should be noted that the decrease in P/Cl selectivity is only 10 to 20% when increasing the cell voltage to 2.0 and 2.5 V while these higher voltages show a 30 to 40% higher phosphate removal efficiency. This slight drop in selectivity may be tolerable if one prioritizes greater removal rates and a smaller unit. **Figure S13a** shows the effluent pH during charge and discharge, suggesting that the effluent pH reached 11.0 at 2.0 V. **Figure S13b** shows the current density versus time profiles under 1.5 V.

To demonstrate the long-term system stability, we conducted cycling performance tests under 2.0 V to balance the high P/Cl selectivity and high phosphate removal efficiency. **Figure 7b** shows that the P/Cl selectivity stabilizes at 1.1 while maintaining a phosphate removal efficiency of at least 31.8% over 30 cycles (which corresponds to 270 minutes). The stable P/Cl selectivity suggests the high long-term stability of 20 wt% Mn_2O_3 composite AEM-BPM MCDI system. We further characterised the carbon cloth electrodes after cycling performance tests using SEM/EDX. As shown in **Figure S14**, the carbon cloth electrode structure before and after cycling tests did not change indicating the cell voltage of 2.0 V over 30 cycles did not corrode the electrodes. **Figure S15** shows the current density versus time profiles under 2 V.

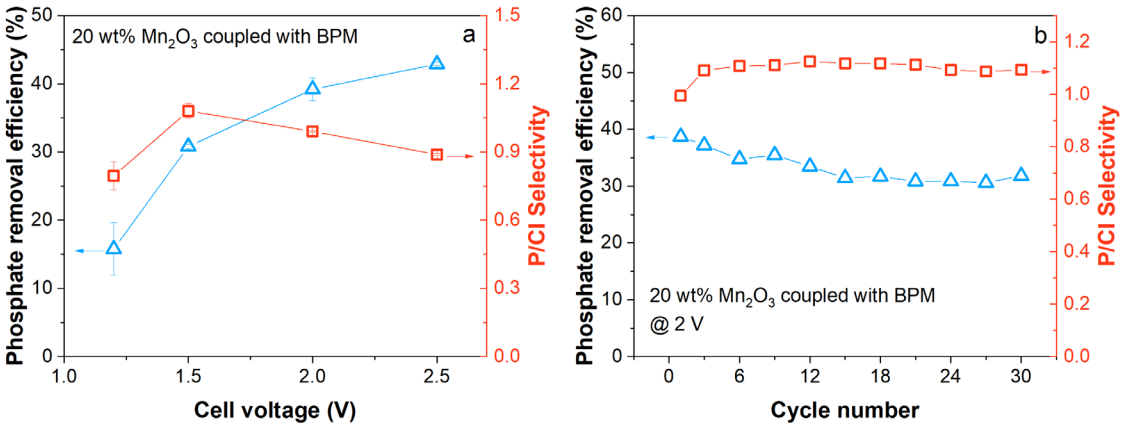

Figure 7. (a) Phosphate removal efficiency and phosphate selectivity under 20 wt% Mn_2O_3 composite AEM coupled with a BPM condition at various cell voltages. (b) MCDI cycling performance of a MCDI unit with a 20 wt% Mn_2O_3 composite AEM and a BPM at 2.0 V.

CONCLUSIONS

In summary, we demonstrate a Mn_2O_3 composite AEM for selective phosphate removal in MCDI and systematically investigate the critical factors affecting the phosphate removal efficiency and phosphate selectivity. These factors include charge mode, solution pH, cell voltage and Mn_2O_3 concentrations (0 to 20 wt%) in the composite AEMs. P/Cl selectivity was improved when operating the MCDI unit under constant voltage charge mode, using a more alkaline feed solution (pH 8.63 versus pH 5.23), applying a lower cell voltage, and utilizing composite AEMs with high Mn_2O_3 concentration. A trade-off was observed between phosphate removal efficiency and phosphate selectivity for the experiments when increasing MCDI cell voltage. Higher cell voltage increases phosphate removal efficiency but decreases P/Cl selectivity. The loss in selectivity with increasing cell voltage can be reduced when using a BPM in the MCDI unit with a composite AEM. This variant displayed a phosphate removal efficiency ≥ 31.8 % and a P/Cl selectivity of 1.1 over 30 cycles. To better understand the role of Mn_2O_3 particles in composite AEMs on phosphate selectivity, we performed static electronic structure calculations. These DFT calculation results revealed that HPO_4^{2-} absorption on Mn_2O_3 composite AEM was 314 kcal/mol more exothermic than that on pristine AEM while Cl^- adsorption on Mn_2O_3 composite AEM was 2.2 kcal/mol less exothermic than that on the pristine AEM. Overall, this work demonstrates that composite AEMs with tuned MCDI operating parameters facilitate selective phosphate removal from model wastewater solutions. The approach of advanced materials, device studies, and DFT calculations provide a strong

framework for selective ion separations that have broad implications to nutrient recovery and securing critical mineral supply chains.

ACKNOWLEDGEMENTS

This work was supported by the U.S. Department of Energy, Office of Science, Basic Energy Sciences, Separation Science program under Award No. DE-SC0022304.

REFERENCES

1. Elser, J.; Bennett, E., A broken biogeochemical cycle. *Nature* **2011,** *478* (7367), 29-31.
2. Lei, Y.; Saakes, M.; van der Weijden, R. D.; Buisman, C. J. N., Electrochemically mediated calcium phosphate precipitation from phosphonates: Implications on phosphorus recovery from non-orthophosphate. *Water Res.* **2020,** *169*, 115206.
3. Le Corre, K. S.; Valsami-Jones, E.; Hobbs, P.; Parsons, S. A., Phosphorus Recovery from Wastewater by Struvite Crystallization: A Review. *Crit. Rev. Environ. Sci. Technol.* **2009,** *39* (6), 433-477.
4. Huang, H.; Zhang, P.; Yang, L.; Zhang, D.; Guo, G.; Liu, J., A pilot-scale investigation on the recovery of zinc and phosphate from phosphating wastewater by step precipitation and crystallization. *Chem. Eng. J.* **2017,** *317*, 640-650.
5. Peng, L.; Dai, H.; Wu, Y.; Peng, Y.; Lu, X., A comprehensive review of phosphorus recovery from wastewater by crystallization processes. *Chemosphere* **2018,** *197*, 768-781.
6. Pan, B.; Han, F.; Nie, G.; Wu, B.; He, K.; Lu, L., New Strategy To Enhance Phosphate Removal from Water by Hydrous Manganese Oxide. *Environ. Sci. Technol.* **2014,** *48* (9), 5101-5107.
7. Wang, J.; Jiang, Y.; Xu, M.; Han, C.; Zhang, L.; Liu, G., Resin-based iron-manganese binary oxide for phosphate selective removal. *Environmental Science and Pollution Research* **2023,** *30* (2), 4642-4652.
8. Zhang, G.; Liu, H.; Liu, R.; Qu, J., Removal of phosphate from water by a Fe–Mn binary oxide adsorbent. *J. Colloid Interface Sci.* **2009,** *335* (2), 168-174.
9. Wu, Z.; Li, X.; Li, H.; Zhang, G., Facile synthesis of novel tremella-like Mn0@Mn2O3 and its exceptional performance on removal of phosphate. *J. Environ. Chem. Eng.* **2021,** *9* (4), 105635.
10. Zhang, Y.; Kinyua, M. N., Identification and classification of the Tetrasphaera genus in enhanced biological phosphorus removal process: a review. *Rev. Environ. Sci. Biotechnol.* **2020,** *19* (4), 699-715.
11. Li, R.; Morrison, L.; Collins, G.; Li, A.; Zhan, X., Simultaneous nitrate and phosphate removal from wastewater lacking organic matter through microbial oxidation of pyrrhotite coupled to nitrate reduction. *Water Res.* **2016,** *96*, 32-41.
12. Li, R.-h.; Cui, J.-l.; Li, X.-d.; Li, X.-y., Phosphorus Removal and Recovery from Wastewater using Fe-Dosing Bioreactor and Cofermentation: Investigation by X-ray Absorption Near-Edge Structure Spectroscopy. *Environ. Sci. Technol.* **2018,** *52* (24), 14119-14128.

13. Dockx, L.; Caluwé, M.; De Vleeschauwer, F.; Dobbeleers, T.; Dries, J., Impact of the substrate composition on enhanced biological phosphorus removal during formation of aerobic granular sludge. *Bioresour. Technol.* **2021,** *337*, 125482.
14. Kolakovic, S.; Freitas, E. B.; Reis, M. A. M.; Carvalho, G.; Oehmen, A., Accumulibacter diversity at the sub-clade level impacts enhanced biological phosphorus removal performance. *Water Res.* **2021,** *199*, 117210.
15. Du, H.; Lung, C. Y. K.; Lau, T.-C., Efficient adsorption, removal and recovery of phosphate and nitrate from water by a novel lanthanum(iii)-Dowex M4195 polymeric ligand exchanger. *Environ. Sci.: Water Res. Technol.* **2018,** *4* (3), 421-427.
16. Tang, W.; He, D.; Zhang, C.; Waite, T. D., Optimization of sulfate removal from brackish water by membrane capacitive deionization (MCDI). *Water Res.* **2017,** *121*, 302-310.
17. Wang, L.; Lin, S., Mechanism of Selective Ion Removal in Membrane Capacitive Deionization for Water Softening. *Environ. Sci. Technol.* **2019,** *53* (10), 5797-5804.
18. Sayed, E. T.; Al Radi, M.; Ahmad, A.; Abdelkareem, M. A.; Alawadhi, H.; Atieh, M. A.; Olabi, A. G., Faradic capacitive deionization (FCDI) for desalination and ion removal from wastewater. *Chemosphere* **2021,** *275*, 130001.
19. Dong, Q.; Guo, X.; Huang, X.; Liu, L.; Tallon, R.; Taylor, B.; Chen, J., Selective removal of lead ions through capacitive deionization: Role of ion-exchange membrane. *Chem. Eng. J.* **2019,** *361*, 1535-1542.
20. Hong, S. P.; Yoon, H.; Lee, J.; Kim, C.; Kim, S.; Lee, J.; Lee, C.; Yoon, J., Selective phosphate removal using layered double hydroxide/reduced graphene oxide (LDH/rGO) composite electrode in capacitive deionization. *J. Colloid Interface Sci.* **2020,** *564*, 1-7.
21. Yang, B.; Yu, J.; Ma, T., A charge-free and membrane-free hybrid capacitive mixing system for salinity gradient energy harvesting. *J. Mater. Chem. A* **2023,** *11* (7), 3388-3398.
22. Tan, C.; He, C.; Tang, W.; Kovalsky, P.; Fletcher, J.; Waite, T. D., Integration of photovoltaic energy supply with membrane capacitive deionization (MCDI) for salt removal from brackish waters. *Water Res.* **2018,** *147*, 276-286.
23. Kulkarni, T.; Al Dhamen, A. M. I.; Bhattacharya, D.; Arges, C. G., Bipolar Membrane Capacitive Deionization for pH-Assisted Ionic Separations. *ACS EST Engg.* **2023,** *3* (12), 2171-2182.
24. Palakkal, V. M.; Rubio, J. E.; Lin, Y. J.; Arges, C. G., Low-Resistant Ion-Exchange Membranes for Energy Efficient Membrane Capacitive Deionization. *ACS Sustain. Chem. Eng.* **2018,** *6* (11), 13778-13786.
25. Bales, C.; Wang, Y.; Lian, B.; He, Z.; Fletcher, J.; Waite, T. D., Predictive performance and costing model for Membrane Capacitive Deionization (MCDI) at operational scale. *Desalination* **2023,** *557*, 116595.
26. Zhang, H.; Wang, Q.; Zhang, J.; Chen, G.; Wang, Z.; Wu, Z., Development of novel ZnZr-COOH/CNT composite electrode for selectively removing phosphate by capacitive deionization. *Chem. Eng. J.* **2022,** *439*, 135527.
27. Shen, Y.-Y.; Hsu, C.-C.; Tsai, S.-W.; Hou, C.-H., Enhanced electrosorption selectivity of phosphate using an anion-exchange resin-coated activated carbon electrode. *J. Colloid Interface Sci.* **2021,** *600*, 199-208.
28. Wang, C.; Li, R.; Xu, Y.; Ma, Z.; Qiu, Y.; Wang, C.; Ren, L.-F.; Shao, J., Effective electrosorption and recovery of phosphorus by capacitive deionization with a covalent organic framework-membrane coating electrode. *Desalination* **2024,** *570*, 117088.
29. Li, G.; Gao, S.; Zhang, G.; Zhang, X., Enhanced adsorption of phosphate from aqueous solution by nanostructured iron(III)–copper(II) binary oxides. *Chem. Eng. J.* **2014,** *235*, 124-131.

30. Zhang, C.; Wang, M.; Xiao, W.; Ma, J.; Sun, J.; Mo, H.; Waite, T. D., Phosphate selective recovery by magnetic iron oxide impregnated carbon flow-electrode capacitive deionization (FCDI). *Water Res.* **2021,** *189*, 116653.
31. Wang, Z.; Xing, M.; Fang, W.; Wu, D., One-step synthesis of magnetite core/zirconia shell nanocomposite for high efficiency removal of phosphate from water. *Appl. Surf. Sci.* **2016,** *366*, 67-77.
32. Zhang, J.; Tang, L.; Tang, W.; Zhong, Y.; Luo, K.; Duan, M.; Xing, W.; Liang, J., Removal and recovery of phosphorus from low-strength wastewaters by flow-electrode capacitive deionization. *Sep. Purif. Technol.* **2020,** *237*, 116322.
33. Xu, L.; Yu, C.; Tian, S.; Mao, Y.; Zong, Y.; Zhang, X.; Zhang, B.; Zhang, C.; Wu, D., Selective Recovery of Phosphorus from Synthetic Urine Using Flow-Electrode Capacitive Deionization (FCDI)-Based Technology. *ACS ES&T Water* **2021,** *1* (1), 175-184.
34. Iddya, A.; Zarzycki, P.; Kingsbury, R.; Khor, C. M.; Ma, S.; Wang, J.; Wheeldon, I.; Ren, Z. J.; Hoek, E. M. V.; Jassby, D., A reverse-selective ion exchange membrane for the selective transport of phosphates via an outer-sphere complexation–diffusion pathway. *Nat. Nanotechnol.* **2022,** *17* (11), 1222-1228.
35. Shrimant, B. K., T.; Hasan, M.; Arnold, C.; Khan, N.; Mondal, A.; Arges, C., Desalting plasma protein solutions by membrane capacitive deionization. *ACS Appl. Mater. Interfaces*, https://doi.org/10.1021/acsami.3c16691.
36. Martos, A. M.; Sanchez, J. Y.; Várez, A.; Levenfeld, B., Electrochemical and structural characterization of sulfonated polysulfone. *Polym. Test.* **2015,** *45*, 185-193.
37. Frisch, M.; Trucks, G.; Schlegel, H.; Scuseria, G.; Robb, M.; Cheeseman, J.; Scalmani, G.; Barone, V.; Petersson, G.; Nakatsuji, H., Gaussian 16 Rev. C. 01, Wallingford, CT. *Wallingford, CT* **2016**.
38. Perdew, J. P.; Burke, K.; Ernzerhof, M., Generalized Gradient Approximation Made Simple. *Phys. Rev. Lett.* **1996,** *77* (18), 3865-3868.
39. Perdew, J. P.; Burke, K.; Ernzerhof, M., Generalized Gradient Approximation Made Simple [Phys. Rev. Lett. 77, 3865 (1996)]. *Phys. Rev. Lett.* **1997,** *78* (7), 1396-1396.
40. Adamo, C.; Barone, V., Toward reliable density functional methods without adjustable parameters: The PBE0 model. *J. Chem. Phys.* **1999,** *110* (13), 6158-6170.
41. Grimme, S.; Antony, J.; Ehrlich, S.; Krieg, H., A consistent and accurate ab initio parametrization of density functional dispersion correction (DFT-D) for the 94 elements H-Pu. *J. Chem. Phys.* **2010,** *132* (15).
42. Becke, A. D.; Johnson, E. R., A density-functional model of the dispersion interaction. *J. Chem. Phys.* **2005,** *123* (15).
43. Johnson, E. R.; Becke, A. D., A post-Hartree–Fock model of intermolecular interactions. *J. Chem. Phys.* **2005,** *123* (2).
44. Johnson, E. R.; Becke, A. D., A post-Hartree-Fock model of intermolecular interactions: Inclusion of higher-order corrections. *J. Chem. Phys.* **2006,** *124* (17).
45. McLean, A. D.; Chandler, G. S., Contracted Gaussian basis sets for molecular calculations. I. Second row atoms, Z=11–18. *J. Chem. Phys.* **1980,** *72* (10), 5639-5648.
46. Krishnan, R.; Binkley, J. S.; Seeger, R.; Pople, J. A., Self-consistent molecular orbital methods. XX. A basis set for correlated wave functions. *J. Chem. Phys.* **1980,** *72* (1), 650-654.
47. Wachters, A. J. H., Gaussian Basis Set for Molecular Wavefunctions Containing Third-Row Atoms. *J. Chem. Phys.* **1970,** *52* (3), 1033-1036.
48. Weigend, F.; Ahlrichs, R., Balanced basis sets of split valence, triple zeta valence and quadruple zeta valence quality for H to Rn: Design and assessment of accuracy. *Phys. Chem. Chem. Phys.* **2005,** *7* (18), 3297-3305.
49. Weigend, F., Accurate Coulomb-fitting basis sets for H to Rn. *Phys. Chem. Chem. Phys.* **2006,** *8* (9), 1057-1065.

50. Scalmani, G.; Frisch, M. J., Continuous surface charge polarizable continuum models of solvation. I. General formalism. *J. Chem. Phys.* **2010,** *132* (11).
51. Hanwell, M. D.; Curtis, D. E.; Lonie, D. C.; Vandermeersch, T.; Zurek, E.; Hutchison, G. R., Avogadro: an advanced semantic chemical editor, visualization, and analysis platform. *J. Cheminform.* **2012,** *4* (1), 17.
52. Jain, A.; Ong, S. P.; Hautier, G.; Chen, W.; Richards, W. D.; Dacek, S.; Cholia, S.; Gunter, D.; Skinner, D.; Ceder, G.; Persson, K. A., Commentary: The Materials Project: A materials genome approach to accelerating materials innovation. *APL Mater.* **2013,** *1* (1).
53. Petousis, I.; Mrdjenovich, D.; Ballouz, E.; Liu, M.; Winston, D.; Chen, W.; Graf, T.; Schladt, T. D.; Persson, K. A.; Prinz, F. B., High-throughput screening of inorganic compounds for the discovery of novel dielectric and optical materials. *Sci. Data* **2017,** *4* (1), 160134.
54. Munro, J. M.; Latimer, K.; Horton, M. K.; Dwaraknath, S.; Persson, K. A., An improved symmetry-based approach to reciprocal space path selection in band structure calculations. *npj Comput. Mater.* **2020,** *6* (1), 112.
55. Singh, A. K.; Zhou, L.; Shinde, A.; Suram, S. K.; Montoya, J. H.; Winston, D.; Gregoire, J. M.; Persson, K. A., Electrochemical Stability of Metastable Materials. *Chem. Mater.* **2017,** *29* (23), 10159-10167.
56. Patel, A. M.; Nørskov, J. K.; Persson, K. A.; Montoya, J. H., Efficient Pourbaix diagrams of many-element compounds. *Phys. Chem. Chem. Phys.* **2019,** *21* (45), 25323-25327.
57. Persson, K. A.; Waldwick, B.; Lazic, P.; Ceder, G., Prediction of solid-aqueous equilibria: Scheme to combine first-principles calculations of solids with experimental aqueous states. *Phys. Rev. B* **2012,** *85* (23), 235438.
58. Horton, M. K.; Montoya, J. H.; Liu, M.; Persson, K. A., High-throughput prediction of the ground-state collinear magnetic order of inorganic materials using Density Functional Theory. *npj Comput. Mater.* **2019,** *5* (1), 64.
59. Ding, H.; Dwaraknath, S. S.; Garten, L.; Ndione, P.; Ginley, D.; Persson, K. A., Computational Approach for Epitaxial Polymorph Stabilization through Substrate Selection. *ACS Appl. Mater. Interfaces* **2016,** *8* (20), 13086-13093.
60. Jain, A.; Hautier, G.; Ong, S. P.; Moore, C. J.; Fischer, C. C.; Persson, K. A.; Ceder, G., Formation enthalpies by mixing GGA and GGA $+$ U calculations. *Phys. Rev. B* **2011,** *84* (4), 045115.
61. Aykol, M.; Dwaraknath, S. S.; Sun, W.; Persson, K. A., Thermodynamic limit for synthesis of metastable inorganic materials. *Sci. Adv.* **2018,** *4* (4), eaaq0148.
62. Tran, R.; Xu, Z.; Radhakrishnan, B.; Winston, D.; Sun, W.; Persson, K. A.; Ong, S. P., Surface energies of elemental crystals. *Sci. Data* **2016,** *3* (1), 160080.
63. de Jong, M.; Chen, W.; Angsten, T.; Jain, A.; Notestine, R.; Gamst, A.; Sluiter, M.; Krishna Ande, C.; van der Zwaag, S.; Plata, J. J.; Toher, C.; Curtarolo, S.; Ceder, G.; Persson, K. A.; Asta, M., Charting the complete elastic properties of inorganic crystalline compounds. *Sci. Data* **2015,** *2* (1), 150009.
64. de Jong, M.; Chen, W.; Geerlings, H.; Asta, M.; Persson, K. A., A database to enable discovery and design of piezoelectric materials. *Sci. Data* **2015,** *2* (1), 150053.
65. Latimer, K.; Dwaraknath, S.; Mathew, K.; Winston, D.; Persson, K. A., Evaluation of thermodynamic equations of state across chemistry and structure in the materials project. *npj Comput. Mater.* **2018,** *4* (1), 40.
66. Zheng, H.; Li, X.-G.; Tran, R.; Chen, C.; Horton, M.; Winston, D.; Persson, K. A.; Ong, S. P., Grain boundary properties of elemental metals. *Acta Mater.* **2020,** *186*, 40-49.
67. Lee, W.-H.; Park, E. J.; Han, J.; Shin, D. W.; Kim, Y. S.; Bae, C., Poly(terphenylene) Anion Exchange Membranes: The Effect of Backbone Structure on Morphology and Membrane Property. *ACS Macro Lett.* **2017,** *6* (5), 566-570.

68. Tang, W.; He, D.; Zhang, C.; Kovalsky, P.; Waite, T. D., Comparison of Faradaic reactions in capacitive deionization (CDI) and membrane capacitive deionization (MCDI) water treatment processes. *Water Res.* **2017,** *120*, 229-237.
69. Choi, J.-H., Comparison of constant voltage (CV) and constant current (CC) operation in the membrane capacitive deionisation process. *Desalination Water Treat.* **2015,** *56* (4), 921-928.
70. Kang, J.; Kim, T.; Jo, K.; Yoon, J., Comparison of salt adsorption capacity and energy consumption between constant current and constant voltage operation in capacitive deionization. *Desalination* **2014,** *352*, 52-57.
71. Wang, L.; Lin, S., Membrane Capacitive Deionization with Constant Current vs Constant Voltage Charging: Which Is Better? *Environ. Sci. Technol.* **2018,** *52* (7), 4051-4060.
72. Sata, T.; Jones, G. N.; Sata, T., *Ion Exchange Membranes: Preparation, Characterization, Modification and Application*. The Royal Society of Chemistry: 2004.
73. Huang, X.; He, D.; Tang, W.; Kovalsky, P.; Waite, T. D., Investigation of pH-dependent phosphate removal from wastewaters by membrane capacitive deionization (MCDI). *Environ. Sci.: Water Res. Technol.* **2017,** *3* (5), 875-882.
74. Hou, C.-H.; Huang, C.-Y., A comparative study of electrosorption selectivity of ions by activated carbon electrodes in capacitive deionization. *Desalination* **2013,** *314*, 124-129.
75. Kumar, A.; Du, F.; Lienhard, J. H. V., Caustic Soda Production, Energy Efficiency, and Electrolyzers. *ACS Energy Lett.* **2021,** *6* (10), 3563-3566.
76. Pärnamäe, R.; Mareev, S.; Nikonenko, V.; Melnikov, S.; Sheldeshov, N.; Zabolotskii, V.; Hamelers, H. V. M.; Tedesco, M., Bipolar membranes: A review on principles, latest developments, and applications. *J. Membr. Sci.* **2021,** *617*, 118538.
77. Kole, S.; Venugopalan, G.; Bhattacharya, D.; Zhang, L.; Cheng, J.; Pivovar, B.; Arges, C. G., Bipolar membrane polarization behavior with systematically varied interfacial areas in the junction region. *J. Mater. Chem. A* **2021,** *9* (4), 2223-2238.

TABLE OF CONTENTS (TOC)